Appl. Phys. B 59, 333–343 (1994)

Applied Physics B Lasers and Optics

Ultrahigh-resolution saturation spectroscopy using slow molecules in an external cell

Ch. Chardonnet, F. Guernet, G. Charton, Ch. J. Bordé

Laboratoire de Physique des Lasers, URA du CNRS No. 282, Université Paris-Nord, Avenue J.-B. Clément, F-93430 Villetaneuse, France
(Fax: +33-1/49 40 3200)

Received 24 November 1993/Accepted 16 May 1994

Abstract. We present the narrowest molecular lines so far recorded in the 10 μm spectral region. A linewidth of 80 Hz (HWHM) has been obtained for the $P(39)A_1^3(-)$ line of OsO_4, by selecting slow molecules ($T_{eff} = 0.6$ K) in saturation spectroscopy at low laser fields (30 nW) and low pressures (2×10^{-6} Torr). In these conditions, the contribution of the fast molecules is greatly reduced because of the finite size of the beam. This method, applied previously to methane at 3.39 μm, is used for the first time in an external cell and improves by a factor 8 the best resolution of our spectrometer. Heterodyne detection and double frequency modulation have been necessary to extract a signal at a contrast of only 10^{-6}. The physical ideas concerning this regime are described and a detailed analysis of the line shape is given.

PACS: 33.80–b, 42.62.Fi

Rovibrational transitions of most molecules have a natural linewidth typically of the order of 1 Hz, and thus can be used to realize very good frequency standards in the infrared. However, it is an extremely difficult task to approach such a resolution: first, because of the pressure broadening which still exceeds 1 Hz at 10^{-7} Torr for most molecules so that either a long external absorption cell or a resonator is required to keep a good contrast; second, the finite transit time of the molecules across the light beam is usually a serious limiting factor in ultrahigh-resolution experiments. As an example, a standing wave generated by a CO_2 laser at 10 μm, with a waist of 3.5 cm, leads to a 700 Hz linewidth (HWHM) for the saturation spectrum of $P(39)A_1^3(-)$ of OsO_4 at 10^{-5} Torr [1], while the pressure broadening is 150 Hz. The combination of the Ramsey separated-field method with saturated absorption gave hopes of significantly longer coherent interaction times but the contrast of the signal is too small in the cell case, so that the method is really adapted only to the molecular beam case [2–4].

Since the size of the laser beam cannot be extended much beyond 30 cm, it is tempting to reduce the velocity of the molecules in order to increase the transit time. Unfortunately, the various laser cooling and trapping techniques which give rise to atomic velocities as low as a few cm/s are not easily applicable to molecules. Up to now, the only alternative is to use saturated absorption at very low power and pressure. In this regime, which will be described in more detail later, the slow molecules are selected optically because of their longer interaction time. This optical selection of slow molecules was first pointed out in the early theories of the line shape in saturation spectroscopy [5–7], and, was demonstrated experimentally for the first time on methane at 3.39 μm [8, 9]. The setup of the Novosibirsk group is an 8 m long cell cooled to 77 K, inside the laser resonator, and the waist of the HeNe laser beam is 15 cm. They exploited the remarkable property of the line shape which becomes peaked and has therefore much narrower derivatives. By detecting the second harmonic of a low modulation frequency, a linewidth of 60 Hz was obtained. This regime has also been investigated at 10 μm with OsO_4, for which a non-derivative linewidth of 3.2 kHz has been observed as the signal was detected by high frequency modulation in transmission of an external Fabry-Perot cavity [10].

We present here the first selective detection of slow molecules observed in an external cell. An unmodulated resonance linewidth of 230 Hz has been measured at 2×10^{-6} Torr while linewidths of 110 Hz and 80 Hz have been obtained at 3×10^{-6} Torr for the detection, respectively, of the first and second harmonic of the low modulation frequency; in these conditions, the pressure broadening is 45 Hz.

1 Qualitative discussion of the optical selection of slow molecules

The theoretical line shape in saturation spectroscopy has been studied in great detail for many years using both weak- and strong-field theories and including transit

effects [7, 11, 12]. The aim of this section is to point out the main features of this line shape under the conditions which are explored in the present experiment and to summarize the important results.

The basic ideas are present in the weak-field theory which includes the Gaussian structure of the laser beam in interaction with the molecules [7]. The applicability of this theory corresponds to a regime where all molecules probe a field much weaker than that corresponding to a $\pi/2$ pulse. This condition is satisfied when

$$\Omega \ll \gamma, \tag{1}$$

where γ is the homogeneous linewidth (in our case, it is essentially the collisional width) and Ω is the angular Rabi frequency. In this regime, the evolution of the linewidth is governed by the relative size of γ and of the transit broadening. For this reason, we introduce the parameter η defined by:

$$\eta = \gamma w_0/u, \tag{2}$$

where w_0 is the laser beam-waist radius and u is the most probable velocity of the molecules. The regime that we consider corresponds to $\eta < 1$, for which the molecules crossing the beam with the velocity u do not suffer any collision. Similarly, we define the parameter θ by

$$\theta = \Omega w_0/u. \tag{3}$$

In the weak field regime (1), $\theta \ll \eta$ and, when η is small, the asymptotic expression for the linewidth (HWHM in s^{-1}) is:

$$\Delta\omega = 1.511\sqrt{\eta}\,\frac{u}{w_0} = 1.511\sqrt{\gamma\,\frac{u}{w_0}}. \tag{4}$$

The second form shows that the linewidth is proportional to the geometrical mean of pressure and transit broadenings and, thus, decreases only as the square root of the pressure. The explanation of this behavior can be found by a study of the contribution to the signal from different transverse velocities v_r. This contribution has very different amplitudes and widths according to the velocity class which is considered. In other words, the line is strongly inhomogeneous.

– First, let us consider the amplitude at resonance. The most important contribution comes from the class with velocity v_r^m:

$$v_r^m \approx \eta u = \gamma w_0, \tag{5}$$

which represents the borderline between slow molecules which are in a collisional regime and the fast ones which are in free flight. The contribution of a single molecule in the collisional regime ($v_r < v_r^m$) is velocity-independent. However, because of the Maxwell-Boltzmann distribution the contribution from each velocity class increases with v_r, reaching a maximum at v_r^m. By contrast, for molecules in free-flight ($v_r > v_r^m$), the contribution scales as $(\theta u/v_r)^4$, so that those which contribute the most are now the slowest ones. One can define an effective temperature corresponding to this dominant velocity class, v_r^m by $T_{eff} = \eta^2 T$, where T is the thermodynamic equilibrium temperature.

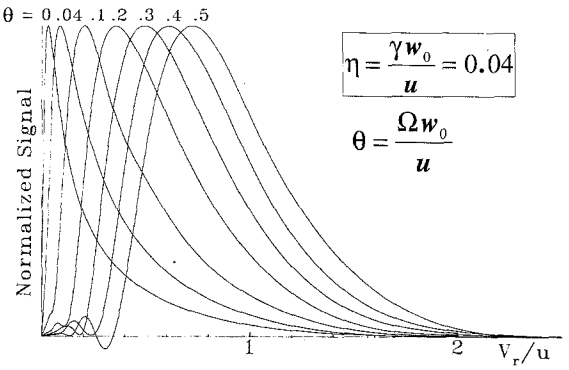

Fig. 1. Normalized contribution of the transverse velocity classes to the saturation signal at resonance for various laser fields. The common value of η is 0.04. For high values of the laser field slow molecules are in a very strong field regime and undergo rapid Rabi oscillations

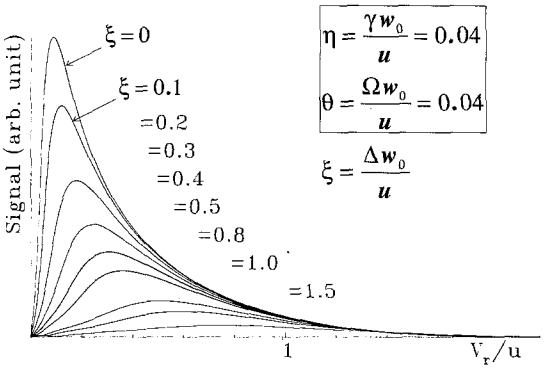

Fig. 2. Contribution of the transverse velocity classes to the saturation signal for various detunings $\Delta = \omega - \omega_0$, in the case $\theta = \eta = 0.04$. ξ is the detuning expressed in transit width units

– Second, let us consider the width of the line for each velocity class. It is clear that, for the first category of molecules ($v_r < v_r^m$), the width is essentially the homogeneous width γ. For the second category ($v_r > v_r^m$), the width is dominated by transit effects and increases with velocity. Therefore, the wings of the resonance come essentially from these fast molecules. This behavior will be confirmed by the asymptotic expressions of the line shape given in the next section for the center and for the wings.

We now discuss how this picture is modified by a larger laser power ($\theta \geq \eta$). In this case, it is the laser field rather than the collisions which selects a dominant velocity class. This class is defined by the condition of an optimum Rabi angle:

$$\theta u/v_r^m \approx 1. \tag{6}$$

In this regime, a strong field theory is required and a quantitative treatment can only be carried through numerically. Condition (6) is illustrated in Fig. 1 which shows the calculated contribution of the transverse velocity classes to the signal versus the laser field at resonance for $\eta = 0.04$. When $\theta = \eta$, the maximum is reached for $v_r^m \approx 2.2\,\eta u$, while for $\theta > \eta$, the maximum shifts linearly with θ. The advantage of the optical selection of slow

molecules is lost as θ increases. If we wish $v_r'^m$ to match the low-field velocity class v_r^m, this requires $\theta \approx \eta$, which is a good compromise between signal and resolution.

Figure 2 shows the contribution of the transverse velocity classes versus detuning in the case $\theta = \eta = 0.04$. The maximum is shifted towards high velocities as the detuning is increased. We conclude, as in weak-field theory, that only the fast molecules contribute to the wings of the resonance.

Figure 3a summarizes the previous results in the weak-field case (which presents the same qualitative features as the case $\theta = \eta$, as we have just seen). This figure illustrates the strongly inhomogeneous character of the line shape with narrow resonances for slow molecules and broad ones for fast molecules. This difference can be exploited by low frequency modulation which amplifies the narrower resonances, as is demonstrated by Figs. 3b, c which display the first and second derivatives, respectively, for each velocity class. This gives a way to emphasize the contribution of the slow molecules and to suppress the wings of the line. This effect is further illustrated on the global line shapes of Figs. 4a–c. In this case,

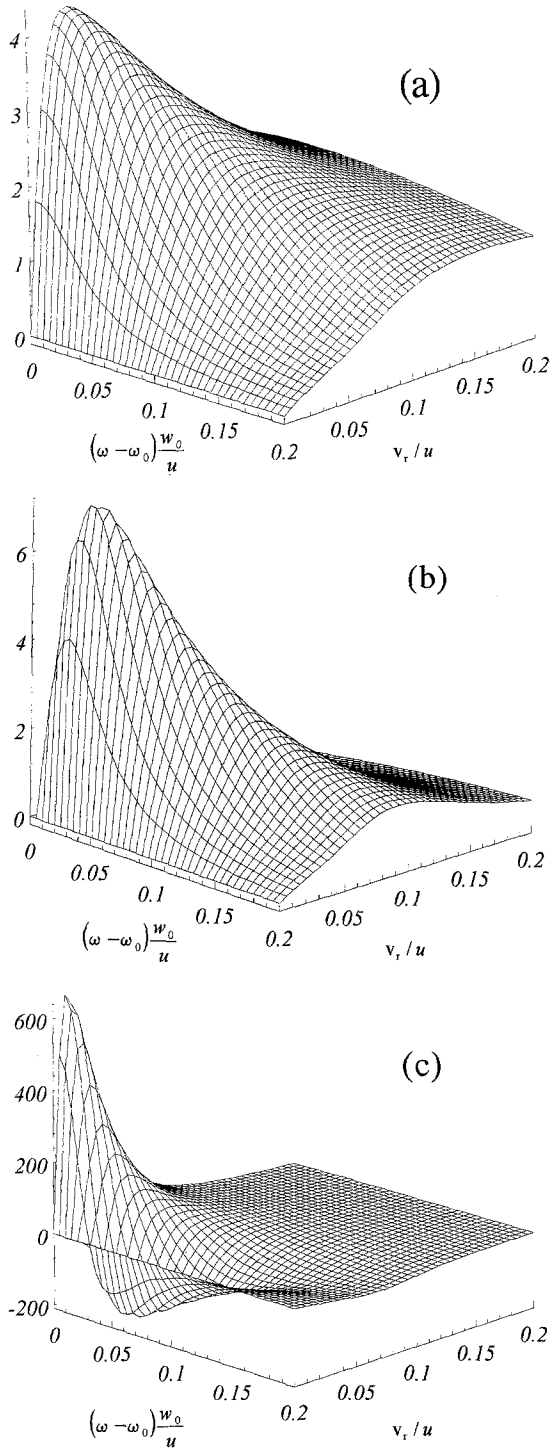

Fig. 3a–c. 3D plots of the weak-field contributions respectively to: (**a**) the saturation signal, (**b**) its first derivative and (**c**) its second derivative, as a function of the reduced transverse velocity v_r/u and of the reduced detuning $\xi = \Delta w_0/u$ ($\eta = 0.04$) (signals are in arbitrary units). Note the disappearance of the wings because fast molecules make practically no contribution to the derivative signals

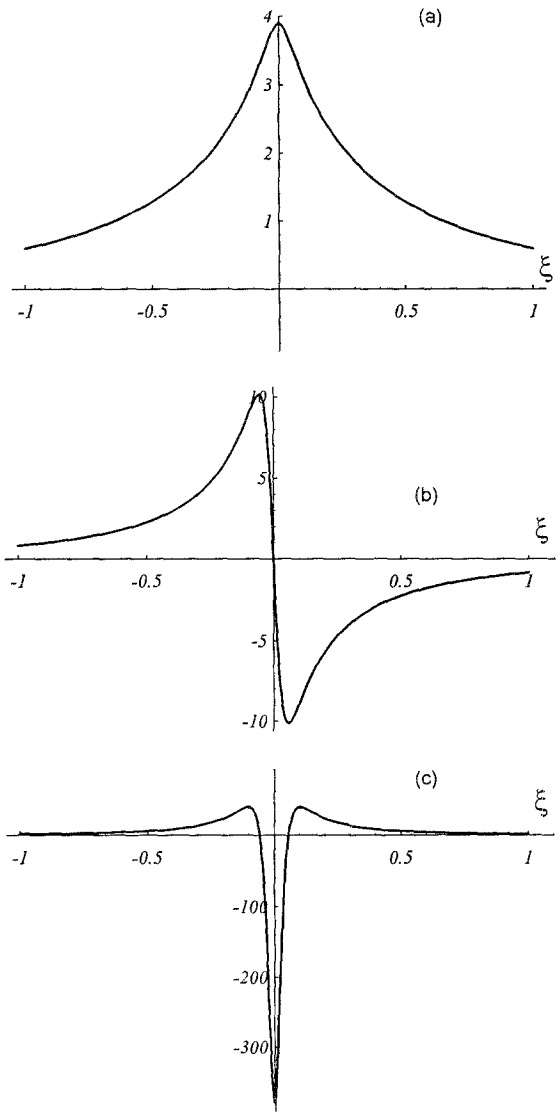

Fig. 4a–c. Global weak-field line shapes after integration over transverse velocities, corresponding to formula (14) ($\eta = 0.04$) (**a**) non-derivative saturation signal, (**b**) first derivative, (**c**) second derivative (signals are in arbitrary units). Note the spectacular narrowing from (**a**) to (**c**)

we expect a linear dependence of the linewidth with pressure.

Another interesting consequence of this regime is a reduction of all the shift mechanisms: the gas-lens effect, the curvature shift, and the pressure shift scale with the linewidth while the second-order Doppler shift $-\delta\omega_R$, determined by

$$\delta\omega_R \approx 1/2\left(\frac{v_r^m}{c}\right)^2 = 1/2\eta^2\left(\frac{u}{c}\right)^2 = 1/2\left(\frac{\gamma w_0}{c}\right)^2, \quad (7)$$

decreases with the square of the pressure and becomes rapidly negligible.

2 Background on the saturation line shape for long-lived systems

This line shape can be calculated either analytically in the weak-field approximation or numerically in the strong-field regime. We shall outline both approaches in this section. From Poynting's theorem, one can see that the change induced by the saturation wave in the absorbed power of the probe wave is given by (see (22), (28), (29) and (74) of [7], but note that indices a and b have been interchanged):

$$\Delta\mathfrak{P} = \frac{\omega}{2}\,\mathrm{Im}\int E\Delta P d^3x = \omega\,\mathrm{Im}\int E\mu\Delta\bar{\varrho}_{ba}d^3x$$

$$= 2\hbar\omega\left(\frac{\mu E_0}{2\hbar}\right)\mathrm{Im}\int\Delta\bar{\varrho}_{ba}U d^3x = 2\hbar\omega\Omega N\Delta\bar{Q}. \quad (8)$$

$N = n_0 L\int dxdy\,UU^*$ is the total number of active molecules in the volume of the interacting laser mode $U(x, y, z) = G(x, z)G(y, z)$ and $\Delta\bar{Q} = \dfrac{2}{\sqrt{\pi}}\dfrac{w_0^2}{\int dxdy\,UU^*}$

$$\times\int_0^{+\infty}d\alpha\alpha e^{-\alpha^2}\int_{-\infty}^{+\infty}d\beta e^{-\beta^2}\,\mathrm{Im}\left[\int\int d\left(\frac{x}{w_0}\right)d\left(\frac{y}{w_0}\right)\frac{\Delta\varrho_{ba}}{n_0}U\right]$$

is the change in the fractional degree of excitation of the optical dipoles. An averaging over a Maxwell-Boltzmann distribution of longitudinal and transverse velocities is performed by integration over the dimensionless variables: $\alpha = v_r/u_\perp$, $\beta = v_z/u_z$ (in a cell $u_\perp = u_z = u$). A final average is performed over spatial coordinates and, for simplicity, we have assumed matched Gaussian beams of waist radius w_0 which do not vary with z over the length L of the cell. The normalization factor $w_0^2/\int dxdy\,UU^*$ is then simply $2/\pi$. $\Delta\varrho_{ba}$ is the change in the off-diagonal density matrix element induced by the saturating field and $\Delta\bar{\varrho}_{ba}$ its average over velocity. Formula (8) demonstrates that each molecule can exchange at most the energy $\hbar\omega$ at a rate $2\Omega = \mu E_0/\hbar$.

The fraction of molecules in β-space, which contribute to the saturation signal, is the ratio of the transit width to the Doppler width $(u_\perp/w_0)/ku_z$. When this factor reaches unity (e.g., in a molecular beam by matching the residual Doppler width and the transit width) a coherent excitation of all molecules leads to $\Delta\varrho_{ba}\approx n_0$, and to $\Delta\bar{Q}\approx 1$. But in a cell and for high resolution, $1/kw_0 \ll 1$, $\exp(-\beta^2)$ can be replaced by unity in the β integral and $\Delta\bar{Q}$ cannot be greater than about $1/kw_0$.

Similarly, in α-space the selective coherent excitation of only those molecules for which $\theta\alpha\approx 1$ will also lead to a reduction factor (absent in the collisional regime $\eta > 1$), as was discussed qualitatively in the previous section and is developed quantitatively below.

2.1 Weak-field theory

Let us first recall the results of the third-order theory [7]:

$$\Delta\bar{Q}^{(3)} = -\frac{\sqrt{\pi}}{kw_0}\theta_p\theta_s^2 g(J_a + J_b), \quad (9)$$

where $\theta_{p,s} = \dfrac{\Omega_{p,s}}{u/w_0}$ are the Rabi frequencies of the probe and saturating beams, respectively, in units of transit width, $g = \int\int dxdy\,U^2U^{*2}/\int\int dxdy\,UU^*$ is a geometrical filling factor introduced in [7] and equal to 1/2 at the beam waist. J_j is the line shape for each recoil peak which can be written as a sum of contributions from the various transverse velocity groups:

$$J_j = \int_0^{+\infty} H_j(\omega - \omega_0 - \Delta\omega_R\alpha^2 + \varepsilon_j\delta, \alpha)\,d\alpha, \quad (10)$$

where $\Delta\omega_R = \omega_0 u^2/2c^2$ is the second-order Doppler shift for the transverse velocity class u, $\delta = \hbar\omega^2/2Mc^2$ is the recoil shift with $\varepsilon_a = -1$ (high-frequency recoil peak), and $\varepsilon_b = +1$ (low-frequency recoil peak). The line shape for each transverse velocity class α is:

$$H_j(\omega - \omega_0, \alpha) = 2\sqrt{\pi}(1+s^2)^{1/2}\exp\left[-\alpha^2 + \left(\frac{\eta_j^2}{4\alpha^2}\right)(1+s^2)\right]$$

$$\times\,\mathrm{Re}\int_0^{+\infty}dX\exp\left[-\alpha^2X^2 - (2\eta_{ba} - \eta_j(1\pm is))X + 2i\xi X\right]$$

$$\times\,\mathrm{erfc}\left[\frac{1\pm is}{(1+s^2)^{1/2}}\alpha X + (\eta_j/2\alpha)(1+s^2)^{1/2}\right], \quad (11)$$

where the notations of [7] have been used:

$$\xi = (\omega - \omega_0)(w_0/u),\ \eta_{ba} = \gamma_{ba}(w_0/u),\ \eta_j = \gamma_j(w_0/u),\ s = 2z/b$$

and the $\pm$ sign corresponds to the direction of the probe wave. In Sect. 1 we assumed that $\eta = \eta_j = \eta_{ba}$.

The line shape (11) is represented in Fig. 3a. It evolves from a broad non-Lorentzian shape dominated by the transit-broadening for large α, to a narrow Lorentzian of halfwidth η_{ba} for $\alpha \ll \eta_j$.

The overall contribution of each velocity class is given by the area under the function H_j in frequency-space:

$$\int_{-\infty}^{+\infty} H_j d\omega = (u/w_0)\pi\sqrt{\pi(1+s^2)}$$

$$\times \exp[-\alpha^2+(\eta_j^2/4\alpha^2)(1+s^2)]\,\mathrm{erfc}\,[(\eta_j/2\alpha)(1+s^2)^{1/2}], \tag{12}$$

which becomes $(u/w_0)(2\pi\alpha/\eta_j)\,e^{-\alpha^2}$ when $\alpha \ll \eta_j$, and $\pi^{3/2}(u/w_0)\times(1+s^2)^{1/2}e^{-\alpha^2}$ when $\eta_j \ll \alpha$. Corresponding formulae for J_j are (Ci(z) and si(z) are the cosine and the sine integral functions [13]):

$$\int_{-\infty}^{+\infty} J_j d\omega = \pi(u/w_0)\sqrt{1+s^2}$$

$$\times[\sin(\eta_j\sqrt{1+s^2})\,\mathrm{Ci}\,(\eta_j\sqrt{1+s^2})-\cos(\eta_j\sqrt{1+s^2})\,\mathrm{si}\,(\eta_j\sqrt{1+s^2})], \tag{13}$$

which gives $\pi u/(w_0\eta_j)$ when $\eta_j \to +\infty$, and $\pi^2(u/w_0)\sqrt{(1+s^2)}/2$ when $\eta_j \to 0$. We now investigate the behavior of the amplitude of the signal as alpha decreases. In the transit-dominated regime ($\alpha > \eta_j$) the area (12) is constant; thus, the width decreases and the amplitude must increase. However, in the collision-dominated regime ($\alpha < \eta_j$) the width tends to η_{ba} as α decreases; hence the area and amplitude both decrease with α. A numerical calculation of the maximum gives $\alpha^m \approx 0.76\eta$ in the case of $\eta = \eta_j = \eta_{ba}$, which confirms the main conclusion of Sect. 1.

If we do not look for the line shape of individual α classes, we can use the following rigorous global line shape (see (84) of [7]):

$$J_j = \eta_j(1+s^2)$$

$$\times\,\mathrm{Im}\left\{\int_0^{+\infty}\frac{dt}{Y}[e^{Z_2}E_1(Z_2)-e^{Z_1}E_1(Z_1)]\exp[2(i\xi-\eta_{ba})t]\right\}, \tag{14}$$

where E_1 is the exponential integral function [13], with $Z_1 = X+iY$, $Z_2 = X-iY$, $X = \eta_j(1\pm is)t$ and $Y = \eta_j\sqrt{1+s^2}\sqrt{1+t^2-2i(\Delta\omega_R w_0/u)t}$. Note that the saturated dispersion line shape is obtained by taking the real part of the previous integral instead of the imaginary part. This line shape is easily calculated numerically using Mathematica [14].

In Appendix C of [7], one of us gave a procedure to calculate this function analytically for small values of η; we recall below the result of [7] and extend it to the first and the second derivatives of the signal in the simplified case where $s=0$ and $\Delta\omega_R = 0$. The line shape consists of four contributions $J_j = J_I + J_{II} + J_{III} + J_{IV}$ given by:

$$J_I = 2\int_0^{+\infty}\frac{\exp[(\eta_j-2\eta_{ba})t]}{\sqrt{1+t^2}}\cos(\eta\sqrt{1+t^2})\cos(2\xi t)$$

$$\times\tan^{-1}\left(\frac{\sqrt{1+t^2}}{t}\right)dt, \tag{15a}$$

$$J_{II} = \Gamma\tan^{-1}\left(\frac{1}{\Xi}\right) = \Gamma[\pi/2-\tan^{-1}(\Xi)], \tag{15b}$$

$$J_{III} = \frac{1}{\Gamma}\ln(\eta_j)J_{II}$$

$$+\frac{1}{2}\mathrm{Im}[E_1(i\mu^+/\sqrt{2})E_1(-i\mu^+/\sqrt{2})-E_1(i\mu^-/\sqrt{2})E_1(-i\mu^-/\sqrt{2})], \tag{15c}$$

$$J_{IV} = \mathrm{Im}\left\{F\left[(1+i)\frac{\eta_j}{\mu^+}\right]-F\left[(1-i)\frac{\eta_j}{\mu^-}\right]\right\}, \tag{15d}$$

where Γ is Euler constant, $\mu^\pm = 2\eta_{ba}-\eta_j-i(2\xi\pm\eta_j)$, $\Xi = \dfrac{(2\eta_{ba}-\eta_j)^2+4\xi^2-\eta_j^2}{2\eta_j(2\eta_{ba}-\eta_j)}$, and F is the dilogarithm function defined by: $F(z) = \sum_{n=1}^{\infty}\dfrac{(-1)^n}{n^2}z^n$, which is itself related to Jonquière's function given in Mathematica [14] by: $F(z) = \mathrm{PolyLog}\,[2,-z]$.

Formulas (15a–d) are valid for small η and for the entire line shape. Close to the line center, J_I can be approximated by [7]:

$$J_I = G-\frac{\pi}{2}\Gamma+\frac{\pi}{2}\ln 2$$

$$-\frac{\pi}{8}\ln(\mu^+\mu^{+*}\mu^-\mu^{-*})+\pi(2\eta_{ba}-\eta_\alpha)(1-2^{-1/2}), \tag{16}$$

where G is the Catalan constant.

Here, for simplicity, we shall take equal relaxation constants $\eta = \eta_j = \eta_{ba}$, in which case J_j can be rewritten in the following analytical form:

$$J_j = G-\frac{\pi\Gamma}{2}+\frac{\pi}{4}\ln 2-\frac{\pi}{2}\ln\eta+\pi\eta-\frac{\pi}{4}\ln|2\zeta^2-2\zeta+1|$$

$$+\mathrm{Im}\{\ln(\sqrt{2}\zeta)\{\ln[1-(1-i)\zeta]-\ln[1-(1+i)\zeta]\}$$

$$+F[-(1-i)\zeta]-F[-(1+i)\zeta]\}, \tag{17}$$

where $\zeta = 1+i\xi/\eta = 1+i(\omega-\omega_0)/\gamma$ is a transit-independent detuning variable. Equation (17) agrees with the integral form (4) of [8] (where one should read $\Gamma^2(Z+1)^2$ instead of $\Gamma^2(Z^2+1)^2$).

This profile provides a good representation of the line shape, as illustrated in Fig. 5, except for the wings. Apart from the frequency-independent terms, $(-\pi/2)\ln\eta+\pi\eta$, this shape is independent of the transit time. The reason is, of course, that the central part of the line shape is dominated by the contribution of slow molecules for which the relaxation is the main broadening mechanism.

J_{II}, J_{III} and J_{IV} contribute essentially to the center of the line and, from the more accurate expression (15a) for J_I, one can derive another formula valid for the wings:

$$J_j = 2\int_0^{+\infty}\frac{\cos 2\xi t}{\sqrt{1+t^2}}\tan^{-1}\left(\frac{\sqrt{1+t^2}}{t}\right)dt. \tag{18}$$

This time we have a universal function of ξ only, which plays the role of an asymptotic envelope for all line shapes as illustrated in Fig. 6. Since only fast molecules contribute to the wings it is not surprising to find a shape

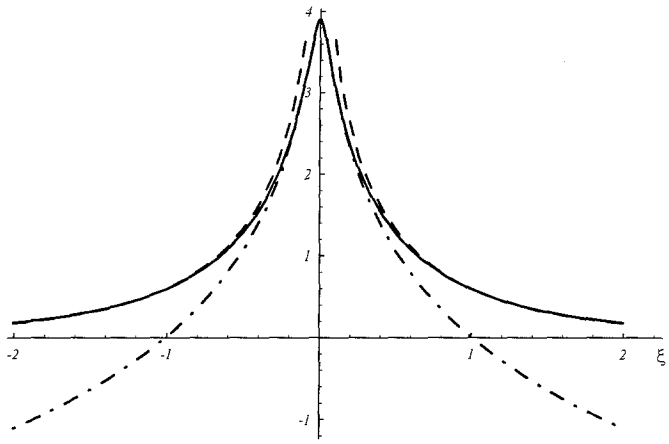

Fig. 5. Comparison of the exact line shape (14) for $\eta_{ba}=\eta_j=\eta=0.04$ with the approximate formulas (17) and (18) which represent the line shape, respectively, close to the line center and in the wings (signals are in arbitrary units)

which depends only upon the transit width. As a matter of fact, formula (18) can also be derived from H_j in the limit of large α:

$$H_j \to 2\sqrt{\pi}\exp(-\alpha^2)\int_0^{+\infty}\exp(-\alpha^2 t^2)\cos(2\xi t)\,\mathrm{erfc}(\alpha t)\,dt. \tag{19}$$

For $|\xi|>1$, we may further approximate the integral (18) by the function:

$$\pi K_0(2|\xi|)-\mathrm{Re}[e^{2\xi}E_1(2\xi)+e^{-2\xi}E_1(-2\xi)], \tag{20}$$

where the Bessel function K_0 becomes very rapidly negligible as $|\xi|$ increases.

The first and second derivatives of J_j are easily derived from the previous formulas. From (17) we find:

$$\frac{dJ_j}{d\xi}=\frac{\pi}{2\eta}\,\mathrm{Im}\left(\frac{2\zeta-1-(4/\pi)\ln(\sqrt{2}\zeta)}{2\zeta^2-2\zeta+1}\right) \tag{21}$$

(for which the first correction would be: $-(\eta/2)\,\mathrm{Arg}\,(2\zeta^2-2\zeta+1)$),

$$\frac{d^2J_j}{d\xi^2}=\frac{2\pi}{\eta^2}$$

$$\times\,\mathrm{Re}\left(\frac{\zeta(1-\zeta)-(1/\pi\zeta)(2\zeta^2-2\zeta+1)+(2/\pi)(2\zeta-1)\ln(\sqrt{2}\zeta)}{(2\zeta^2-2\zeta+1)^2}\right). \tag{22}$$

To this approximation these derivative line shapes depend only upon $(\omega-\omega_0)/\gamma$, which means that these line shapes are universal functions, independent of the transit time. One should keep in mind that the actual experimental derivative signals are plotted as functions of Δ and not of ξ, so that the amplitude factors of these derivatives of J_j involve only $1/\gamma$. Figures 7a, b display and compare these functions with the derivatives of the exact formula (14). The agreement is excellent everywhere for the second derivative. For the first derivative good agreement is limited to the central part of the line shape between the extrema while the derivative of (18) is preferred to represent the wings:

$$\frac{dJ_j}{d\xi}\approx -4\int_0^{+\infty}\frac{t\sin 2\xi t}{\sqrt{1+t^2}}\tan^{-1}\left(\frac{\sqrt{1+t^2}}{t}\right). \tag{23}$$

The approximate line shapes (17, 21, 22) greatly facilitate the study of the linewidth versus pressure (η). Formula (17) yields a closed-form expression for the halfwidth [7]: $2^{-1/4}\exp[(3G/\pi)-(\Gamma/2)]\sqrt{\eta}$. Since formulas (21) and (22) are functions which depend only on $(\omega-\omega_0)/\gamma$, it is clear that the widths of the derivative line shapes will be linear functions of γ and hence of η. One finds $1.443\eta\approx\eta/\ln 2$ for the half peak-to-peak width of the first derivative and 0.634η for the halfwidth at half-maximum of the second derivative. The gain in resolution is clear on Fig. 8, which displays the three respective linewidths versus η.

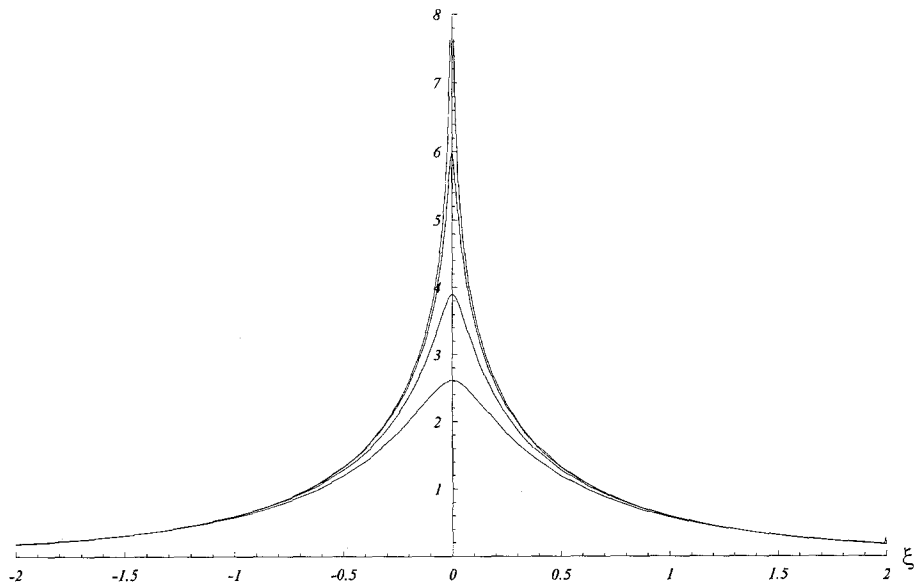

Fig. 6. Comparison of the exact line shapes (14) for $\eta=0.1$, 0.04, 0.01 (from bottom to top) with the universal approximate formula (18), which diverges at line center

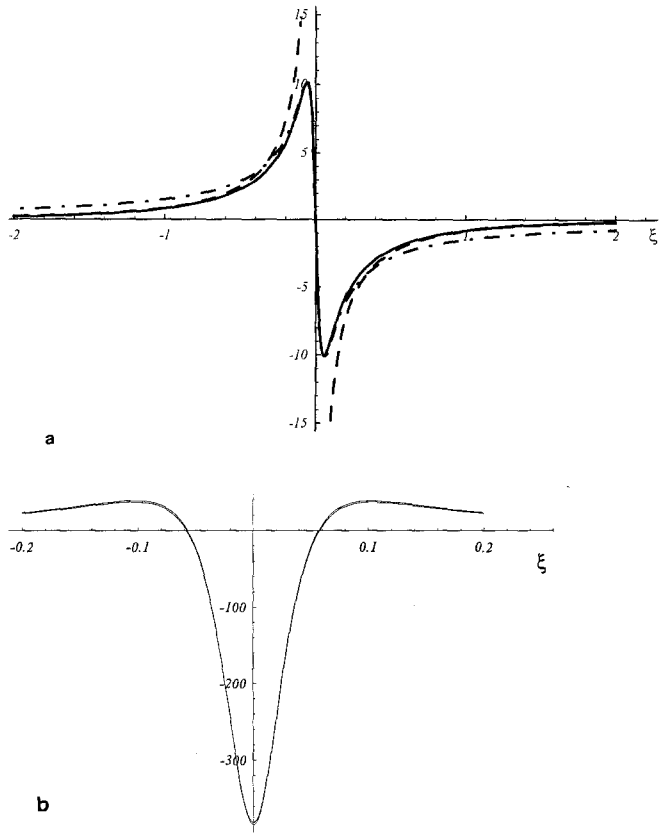

Fig. 7. **a** Comparison of the exact first-derivative line shape, deduced from (14), for $\eta = 0.04$ with the approximate formula (21) and (23) which represent the line shape, respectively, close to the line center and in the wings. **b** Comparison of the exact second-derivative line shape, deduced from (14), for $\eta = 0.04$ with the approximate formula (22). These two curves are almost indistinguishable

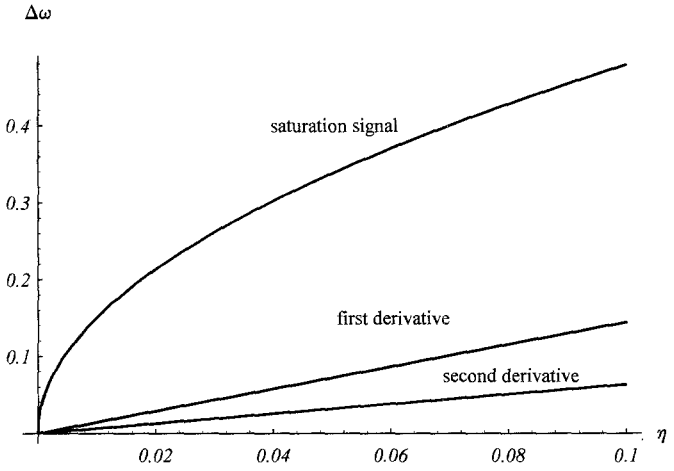

Fig. 8. Linewidths, in unit of transit width (u/w_0), of the saturation signal and its first and second derivatives as a function of η

2.2 Strong-field theory

A realistic description of the line shape requires account to be taken of the strong-field aspects since slow molecules are always more or less in the situation of a strong field regime, as is well illustrated in Fig. 1. A numerical

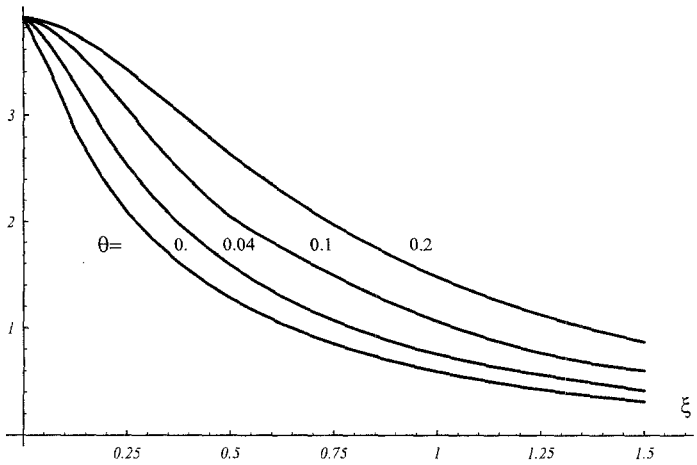

Fig. 9. Normalized global line shapes for $\eta = 0.04$ and for $\theta = 0$, 0.04, 0.1, 0.2 which show the power broadening of the saturation signal. The width for $\theta = 0.1$ is almost multiplied by 2 and the peaked character of the line disappears very rapidly as θ increases

program which computes the density matrix in this case was developed as early as 1973 [12, 15]. This program gives (the coordinate z has been omitted for simplicity):

$$\text{Shape}(y) = kw_0 \int_0^{+\infty} d\alpha\alpha e^{-\alpha^2} \int_{-\infty}^{+\infty} d\beta \int_{-\infty}^{+\infty} d\left(\frac{x}{w_0}\right) \times \text{Im}\left[\frac{\Delta\varrho_{ba}(x, y)}{n_0} G(x)G(y)\right], \quad (24)$$

from which we obtain:

$$\Delta\bar{Q} = \frac{2}{\sqrt{\pi}} \frac{u/w_0}{ku} w_0 \int_{-\infty}^{+\infty} dy G(y)\,\text{Shape}(y) / \int dx dy\, UU^*. \quad (25)$$

In the weak field limit, $\text{Shape}(y) = \text{Shape}(0) G^3(y)$ and

$$\Delta\bar{Q}^{(3)} = \frac{2}{\sqrt{\pi}} \frac{u/w_0}{ku} w_0\,\text{Shape}(0) \int_{-\infty}^{+\infty} dy G^4(y) / \int dx dy\, UU^*. \quad (26)$$

Comparison with (9) shows that, in this limit, $\text{Shape}(0) = (\pi\sqrt{\pi}/4)(J_a + J_b)\theta_p\theta_s^2$. The program Shape has been used to calculate the curves of Figs. 1 and 2 and we have plotted Shape (0) for several values of the field in Fig. 9 to illustrate the fast saturation broadening of the resonance. In order to obtain a complete comparison with the experiment, the integration over the transverse coordinate y has to be performed and the influence of the various modulations should be taken into account. This study will be presented in another paper.

3 Experimental results

The selection of slow molecules requires low pressure and low saturation power. These two conditions lead to a

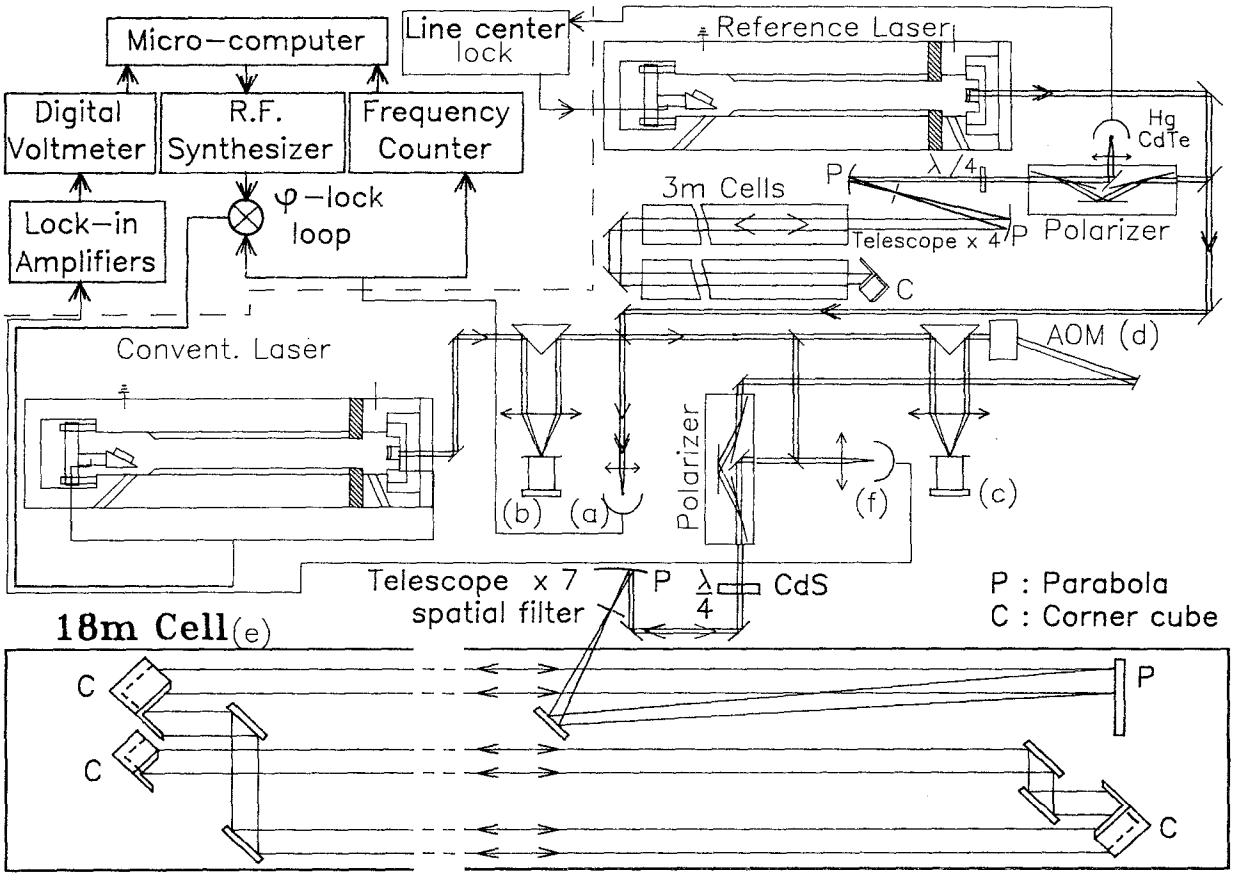

Fig. 10a–f. Experimental arrangement, (**a**) beat note detector for the phase-lock loop, (**b**) first PZT-mounted mirror and cat's eye for the high frequency modulation, (**c**) second PZT-mounted mirror for dephasing compensation of the modulation between local oscillator and probe beams, (**d**) AOM which shifts the probe beam frequency by 40 MHz, (**e**) absorption cell illuminated by a collimated beam of waist radius $w_0 = 3.5$ cm and of total (back and forth) path length of 108 m, (**f**) 40 MHz beat-note detector for the heterodyne detection

severe reduction of the signal and hence the detectivity becomes the crucial point in the experiment. When the absorption cell is placed inside the laser cavity, with operating conditions just above threshold as was done with methane at 3.39 μm using a HeNe laser [8, 9], a very powerful amplification of the signal is obtained (10^5 by comparison with an external cell), but this technique does not have general applicability. The use of an external Fabry-Perot cavity [10] increases the contrast by the finesse, but the waist cannot be much larger than a few mm and an additional stabilization system is required. The choice of the external cell is simpler, more general, and allows more flexibility in changing the parameters and the modulation techniques. The price to pay, however, is a very weak contrast.

The basic structure of our spectrometer has been described earlier [10, 16, 17] and Fig. 10 shows the essential new features introduced for this experiment. The local oscillator is a low-pressure CO_2 laser which is locked to the third derivative of a saturation signal. Here we employed a molecular line in OsO_4 of width about 100 kHz. The spectral purity is 10 Hz, the long-term drift is a few Hz/min, but on a time scale of a few minutes fluctuations in the frequency of several tens of Hz have been detected and arise probably from residual interference fringes in the optical train. A second laser, which is frequency-shifted from the first laser with a phase-lock loop including a tunable synthesizer, is expanded into the 18 m cell up to a waist of 3.5 cm, and generates a triple standing wave. The saturation signal is detected directly on the retroreflected beam.

For the detection of signals as weak as $10^{-14} - 10^{-15}$ W in the middle infrared, heterodyne detection is necessary to overcome the detector noise. For that purpose, a beam splitter divides the laser beam into two parts. The first beam, with a power of 0.5 mW, is used for the local oscillator. The second one is shifted in frequency by 40 MHz through an Acousto-Optic Modulator (AOM) and, after a round trip in the cell, is recombined with the local oscillator beam. Both are then directed towards a HgCdTe detector in order to detect the beat note at 40 MHz. After preamplification, a balanced mixer gives rise to an electrical voltage proportional to the product of the powers of both beams. In order to transpose the signal outside the technical noise region of the laser (0 – 20 kHz), a modulation frequency, $f_h = 58$ kHz, is applied to the laser beam before the beam splitter. For this purpose, a PZT-mounted mirror is placed at the focus of a cat's eye which avoids any angular modulation of the beam. The optical adjustment is tuned exactly by

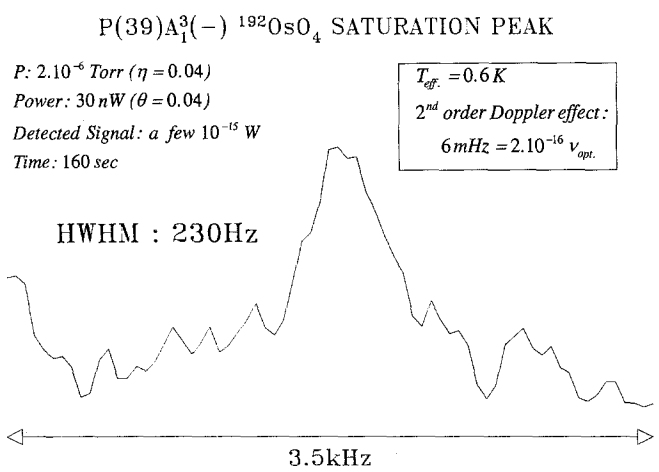

Fig. 11. Saturation signal for the $^{192}OsO_4$ $P(39)A_1^3(-)$ line, for $\theta = \eta = 0.04$, detected by a high frequency modulation technique

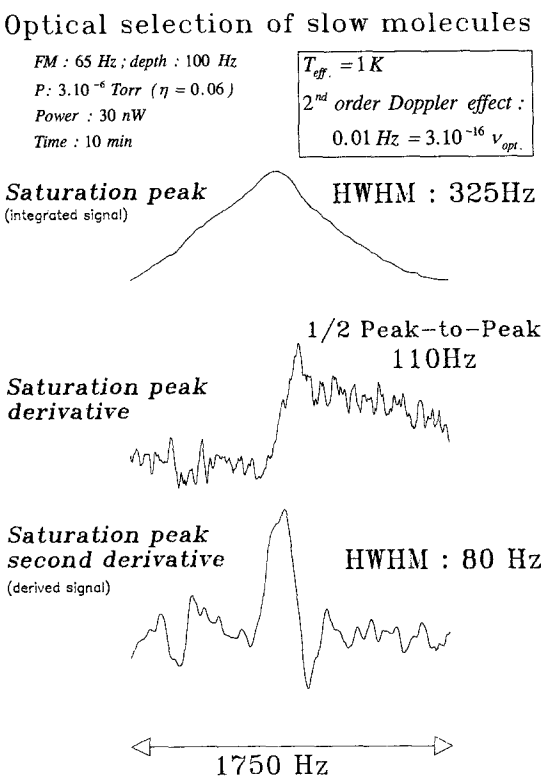

Fig. 12. Saturation signal for the $^{192}OsO_4$ $P(39)A_1^3(-)$ line, for $\theta = 0.04$ and $\eta = 0.06$, detected by a double modulation technique (see text). The line shape is essentially the first derivative of the unmodulated line. The integrated and second-derivative signals are obtained numerically from the original first-derivative spectrum and illustrate the narrowing of the derivative line shapes

cancelling any induced AM. The same setup is implemented just on the probe beam. An extra modulation at the same frequency f_h, but with a different phase, is applied in order to compensate a small but significant dephasing due to the large path-length difference between the two beams before the detector. This high frequency modulation technique gives rise to a signal with exactly the same shape as an unmodulated signal. Figure 11 exhibits such a signal recorded at an OsO_4 pressure of 2×10^{-6} Torr with a saturation power of 30 nW. These values correspond to $\theta = \eta = 0.04$ and to a linewidth of 230 Hz (HWHM) which is in good agreement with the expected value, being only 20% larger than the linewidth in the weak-field regime. The effective temperature associated with the top of the resonance is 0.6 K while the corresponding transverse velocity is 6 m/s. The second-order Doppler shift is $2 \times 10^{-16}\, \nu_{opt}$. This spectrum comprises 150 points and was recorded in 160 s. It corresponds to a signal of a few 10^{-3} pW, and to a contrast of the order of 10^{-7}. The signal-to-noise ratio is half that allowed by the shot-noise limit, and the heterodyne detection improves the detectivity by more than two orders of magnitude. Spectral analysis of the noise around the modulation frequency reveals a technical noise which extends up to about 10 Hz and which results in slow baseline fluctuations. The main origin of this noise might come from the small relative motion between the optical table, which has a vibration frequency of a few Hz, and the large cell, thus affecting the overlapping of the probe and local oscillator beams.

As explained in the previous part of this paper, the first and second derivatives of the saturation line shape should be much narrower than the non-derivative line shape. In order to obtain a derivative line shape, one should apply a modulation with a frequency lower than the linewidth. In our case, this would imply a modulation in a frequency region where the laser technical noise is, by far, too important. In order to keep both a derivative line shape and a reasonable signal-to-noise ratio, two frequency modulations are used. The high modulation frequency f_h, is maintained and, in addition, we apply a second low frequency modulation f_l to the laser cavity length. The first one transfers the signal outside the laser technical noise region. A first lock-in amplifier detects the f_h component of the signal (as in the previous experiment) with a time constant short enough to keep the f_l component of the demodulated signal. This signal is the same as that obtained in the previous experiment, but it is now modulated at a frequency f_l. After demodulation at f_l by a second lock-in amplifier, we recover the first derivative of the saturation signal, possibly broadened by modulation. Although the use of a second modulation partly reduces the signal, a remarkable observation is that, by choosing a frequency outside the extra technical noise region ($f_l > 20$ Hz), we could eliminate completely any baseline fluctuation, which had distorted the line shape when it was not well averaged in the previous series of experiments. A more detailed description and analysis of the different modulation and detection techniques will be given in another paper [18].

Figure 12 shows an example of the highest resolution that we could achieve with this technique. A linewidth of 110 Hz (half-peak-to-peak) has been obtained at a pressure of 3×10^{-6} Torr ($\eta = 0.06$) and a saturation power of 30 nW ($\theta = 0.04$) for a modulation frequency of 65 Hz and a modulation depth of 100 Hz. At that pressure, the linewidth in the weak-field regime is 70 Hz, the extra width being due to saturation and modulation broadenings. In order to show the improvement obtained by the

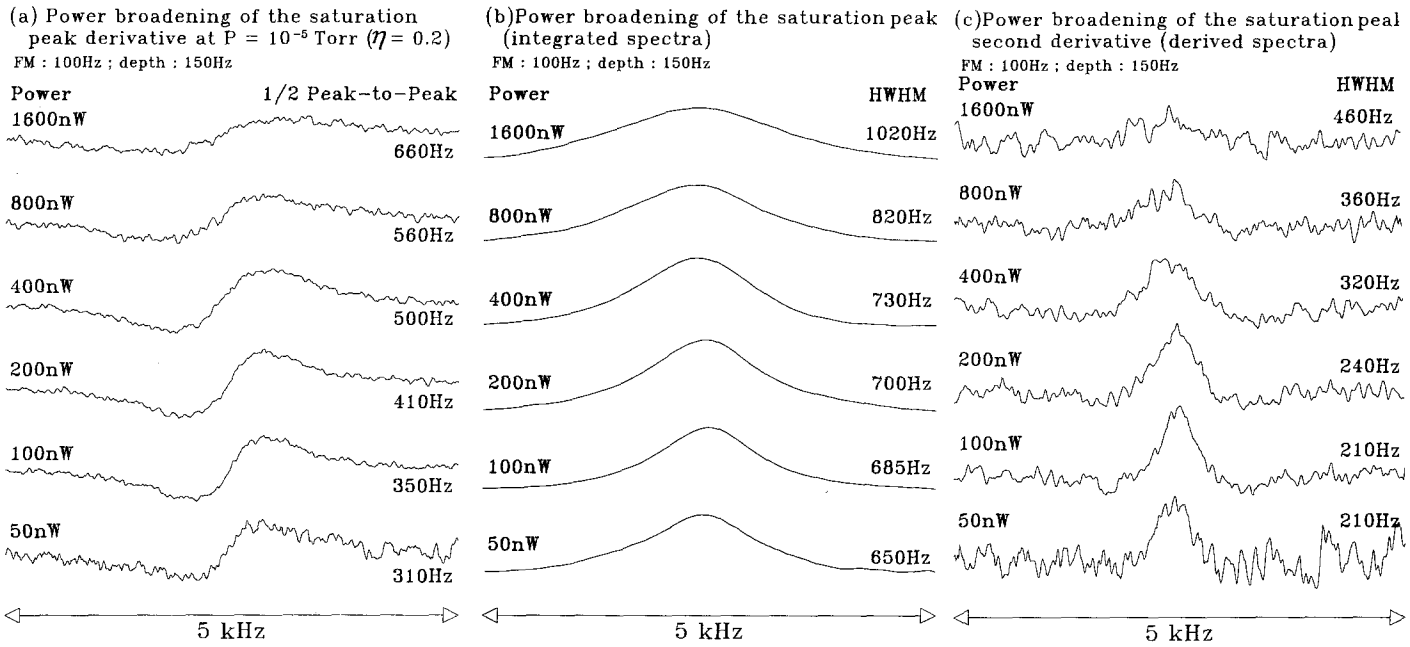

Fig. 13a–c. Power broadening of the saturation peak at an OsO_4 pressure of 10^{-5} Torr ($\eta = 0.2$) in the range $\theta = 0.05 - 0.3$. (**a**) Signals recorded by the double modulation technique, (**b**) numerically integrated signals, (**c**) numerically derived signals

use of the derivative line shapes, we have integrated and derived the experimental spectrum (for the derivation, a numerical filter has been applied in order to reduce the noise). The integrated signal restores the unmodulated saturation signal; it is 3 times wider than the original derivative signal but only 25% wider than the theoretical saturation peak in the weak-field limit. Finally, despite the filtering operation, we obtain a narrower derivative signal (corresponding to the second-harmonic detection) of 80 Hz HWHM. These results illustrate that only the center of the resonance, which is effectively produced by the slow molecules, is detected by the low frequency modulation while faster molecules responsible for the wings of the unmodulated signal cease to contribute.

This effect is illustrated in a different way on Fig. 13, which displays the results of an experiment performed at 10^{-5} Torr. Using the double modulation technique, we have recorded the signal for various saturation powers (Fig. 13a). As for Fig. 12, we have plotted the integrated (Fig. 13b) and derived (Fig. 13c) signals. This time, the modulation frequency is 100 Hz and the modulation depth is 150 Hz. While a reduction factor of 2.2 is achieved for the width of the derived lines (Fig. 13a and 13c), a reduction factor of only 1.55 is obtained for the "unmodulated" line (Fig. 13b). In addition, noting that each spectrum is recorded with the same accumulation time (3 min), it is remarkable to observe on Figs. 13a, c the improvement in signal-to-noise ratio achieved by a reduction of the saturation power by more than one order of magnitude. This very surprising observation is a direct consequence of the increasingly peaked character of the saturation line shape as the power decreases, which is clearly visible on Fig. 13b. We recognize here the behavior predicted by Fig. 9.

As a final illustration of the power of the method, we give in Fig. 14 the first resolved hyperfine structure of an isolated Q line of the ν_3 band of SF_6.

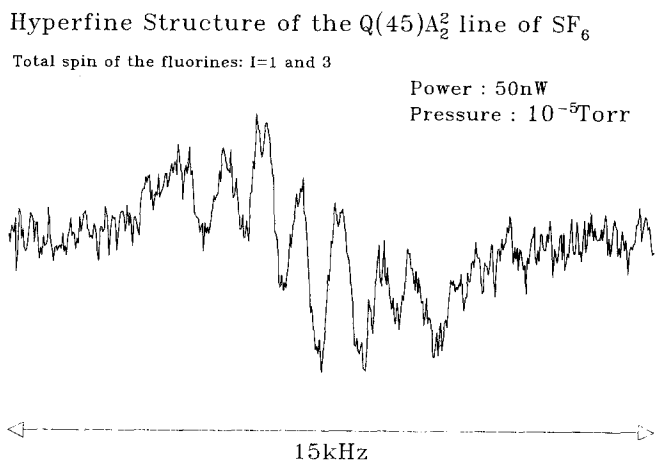

Fig. 14. Saturation spectrum of the $Q(45)A_2^2$ line of the ν_3 band of SF_6, recorded at a pressure of 10^{-5} Torr and with a power of 30 nW. We have fitted the resonances with derivatives of Lorentzians having a halfwidth at half-maximum equal to 560 Hz. Agreement with the predicted structure [19] is almost perfect

4 Conclusion

This study exhibits the first results of an optical selection of slow molecules by saturation spectroscopy in a cell external to any resonator. Despite the small contrast of the signal, we have obtained almost the same linewidth as in the case of the methane experiment even though our laser beam waist is 4.5 times smaller. This is a confirma-

tion that, in the low pressure and low saturation power regime, transit effects do not contribute any more to the linewidths of the derivative signals which are governed by pressure alone. Within this context, a large size of the laser beam is still an interesting consideration but only because the signal increases rapidly with w_0, due both to a volume effect and to the selection of a faster and hence more numerous transverse velocity class.

Our new result constitutes an improvement of the resolving power of our spectrometer by a factor 8 which opens new perspectives for the study of hyperfine structures or large amplitude motions in molecular spectroscopy. With the present resolution, it will be possible to resolve the recoil doublet for light molecules such as NH_3. However, much more effort is still required in order to reach the natural linewidth.

Frequency metrology is another field for which this method of optical selection of slow molecules appears very promising. In this regime of low pressure and low power, the second-order Doppler effect decreases as the square of the linewidth and the value of 5 mHz estimated for our experiment is a negligible correction. Other systematic effects (curvature shift, gas-lens effect, etc.) [12] vary linearly with the linewidth, and an upper value of 1 Hz ($3 \times 10^{-14} \nu_{opt.}$) can be given. In the present conditions, the influence of the unbalance between unresolved recoil components (separated by 14 Hz for OsO_4) on the apparent line center is expected to be negligible, but it should be considered seriously for future higher resolution experiments. Finally, the signal-to-noise ratio now available yields an accuracy of a few Hz on a time scale of one second.

References

1. Ch.J. Bordé, J. Bordé, Ch. Bréant, Ch. Chardonnet, A. Van Lerberghe, Ch. Salomon: In *Laser Spectroscopy VII,* ed. by T.W. Hänsch, Y.R. Shen, Springer Ser. Opt. Sci., Vol. 49 (Springer, Berlin, Heidelberg 1988) p. 108
2. Ch. Salomon, Ch. Bréant, Ch.J. Bordé, R.L. Barger: J. Phys. **42**, C8-3 (1981)
3. Ch. Salomon, S. Avrillier, A. Van Lerberghe, Ch.J. Bordé: In *Laser Spectroscopy VI,* ed. by H.P. Weber, W. Lüthy, Springer Ser. Opt. Sci., Vol. 40 (Springer, Berlin, Heidelberg 1983) p. 150
4. Ch.J. Bordé, S. Avrillier, Ch. Salomon, A. Van Lerberghe, Ch. Bréant, D. Bassi, G. Scoles: Phys. Rev. A **30**, 1836 (1984)
5. Ch.J. Bordé, J.L. Hall: In *Proc. 2nd Symp. on Gas Laser Physics* (Academy of Science of the USSR, Department of General Physics and Astronomy, Moscow 1975) pp. 105–106
6. E.V. Baklanov, B.Y. Dubetskii, V.M. Semibalamut, E.A. Titov: Sov. J. Quant. Electron. **5**, 1374 (1976)
7. Ch.J. Bordé, J.L. Hall, C.V. Kunasz, D.G. Hummer: Phys. Rev. **14**, 236 (1976)
8. S.N. Bagayev, A.E. Baklanov, V.P. Chebotayev, A.S. Dychkov: Rev. Roum. Phys. **33**, 361 (1988)
9. S.N. Bagayev, V.P. Chebotayev, A.K. Dmitriyev, A.E. Om, Y.V. Nekrasov, B.N. Skvortsov: Appl. Phys. B **52**, 63 (1991)
10. A. Clairon, O. Acef, Ch. Chardonnet, Ch.J. Bordé: In *Frequency Standards and Metrology,* ed. by A. de Marchi (Springer, Berlin, Heidelberg 1989) pp. 212–220
11. Ch.J. Bordé, Ch. Chardonnet, D. Mayou: In *Laser Spectroscopy VIII,* ed. by W. Persson, S. Svanberg, Springer Ser. Opt. Sci., Vol. 55 (Springer, Berlin, Heidelberg 1989) pp. 381–385
12. Ch.J. Bordé: In *Frequency Standards and Metrology,* ed. by A. de Marchi (Springer, Berlin, Heidelberg 1989) pp. 196–205
13. M. Abramowitz, I.A. Stegun (eds.): *Handbook of Mathematical Functions* (Dover, New York 1965)
14. S. Wolfram: *Mathematica, a System for doing Mathematics by Computer* (Addison-Wesley, Redwood City, CA 1988)
15. Ch.J. Bordé, C.V. Kunasz, J.L. Hall: Unpublished
16. Ch.J. Bordé: Revue du Cethedec **NS 83**-*1,* 1 (1982)
17. O. Pfister, F. Guernet, G. Charton, Ch. Chardonnet, F. Herlemont, J. Legrand: J. Opt. Soc. Am. B **10**, 1521 (1993)
18. F. Guernet, G. Charton, Ch. Chardonnet, Ch.J. Bordé: (in press)
19. Ch. Chardonnet, Ch.J. Bordé: Europhys. Lett. **9**, 527 (1989)